What Can the Internal Variability of CMIP5 Models Tell Us about Their Climate Sensitivity?

NICHOLAS J. LUTSKO

Department of Earth, Atmospheric, and Planetary Sciences, Massachusetts Institute of Technology, Cambridge, Massachusetts

KEN TAKAHASHI

Instituto Geofisico del Peru, Lima, Peru

(Manuscript received 27 October 2017, in final form 19 March 2018)

ABSTRACT

The relationship between climate models' internal variability and their response to external forcings is investigated. Frequency-dependent regressions are performed between the outgoing top-of-atmosphere (TOA) energy fluxes and the global-mean surface temperature in the preindustrial control simulations of the CMIP5 archive. Two distinct regimes are found. At subdecadal frequencies the surface temperature and the outgoing shortwave flux are in quadrature, while the outgoing longwave flux is linearly related to temperature and acts as a negative feedback on temperature perturbations. On longer time scales the outgoing shortwave and longwave fluxes are both linearly related to temperature, with the longwave continuing to act as a negative feedback and the shortwave acting as a positive feedback on temperature variability. In addition to the different phase relationships, the two regimes can also be seen in estimates of the coherence and of the frequency-dependent regression coefficients. The frequency-dependent regression coefficients for the total cloudy-sky flux on time scales of 2.5 to 3 years are found to be strongly ($r^2 > 0.6$) related to the models' equilibrium climate sensitivities (ECSs), suggesting a potential "emergent constraint" for Earth's ECS. However, $O(100)$ years of data are required for this relationship to become robust. A simple model for Earth's surface temperature variability and its relationship to the TOA fluxes is used to provide a physical interpretation of these results.

1. Introduction

The energy balance for Earth's response to a radiative perturbation can be approximately written as

$$N(t) = F(t) - \beta T(t), \tag{1}$$

where N is the net top-of-atmosphere (TOA) radiative flux, F is the radiative perturbation, β is a radiative restoring coefficient (also commonly referred to as the climate feedback parameter), T is the global-mean surface temperature anomaly, and t is time. Separating into forced components (subscript F) and components of internal variability (subscript I) gives

$$N_F(t) + N_I(t) = F(t) - \beta_F T_F(t) - \beta_I T_I(t), \tag{2}$$

where we have assumed that the forced components and the internal variability components can be added linearly. In this study we investigate the relationship between β_F and β_I in a subset of the models participating in the phase 5 of the Climate Model Intercomparison Project (CMIP5). We also investigate whether β_I is related to the models' equilibrium climate sensitivity (ECS), the temperature change for a doubling of CO_2: $\mathrm{ECS} \equiv F_{2\mathrm{xCO_2}}/\beta_F$. In relating the internal variability of the models to their responses to external forcings, our study can be thought of as a heuristic application of the fluctuation–dissipation theorem, which has been used in a number of climate contexts recently (e.g., Gritsun and Branstator 2007; Ring and Plumb 2008; Cooper and Haynes 2011; Lutsko et al. 2015).

The two βs are not assumed equal. In particular, β_I is likely to be a function of frequency, as the relationship

Denotes content that is immediately available upon publication as open access.

Corresponding author: Nicholas Lutsko, lutsko@mit.edu

DOI: 10.1175/JCLI-D-17-0736.1

between N_I and T_I changes on different time scales. Moreover, β_I is not necessarily a feedback parameter. On some time scales N_I and T_I may be linearly related, with temperature anomalies damping N_I anomalies, but on other time scales T_I anomalies and N_I anomalies may not be linearly related. For instance, temperature anomalies could force radiative anomalies at a particular frequency ω_1, so that $dN_I(\omega_1)/dt \propto T_I(\omega_1)$, in which case $\beta_I(\omega_1)$ is a complex number. Hence we simply define β_I as the coefficient relating N_I anomalies and T_I anomalies at a given frequency.

Because of the frequency dependence of β_I, we cannot estimate it by performing linear regression of the time series of N_I versus the time series of T_I, and instead must work in the frequency domain. The aim is to find a particular range of frequencies in which the estimates of β_I are correlated with estimates of β_F and ECS (we assume that β_F is independent of frequency); such a relationship could exist even if β_I is not a feedback parameter at these frequencies.

If this frequency range does exist then it would constitute an ''emergent constraint'' on Earth's sensitivity, particularly if β_I is proportional to β_F and/or ECS at high frequencies. An emergent constraint is a correlation across climate models between a potentially observable variable and the models' responses to an external forcing. A well-known example is the strong relationship between the seasonal cycle in surface albedo over Northern Hemisphere land and the response of surface albedo over Northern Hemisphere land to increased greenhouse gas concentrations (Hall and Qu 2006). Here, Earth's β_I could potentially be estimated from satellite observations of T and N, and so Earth's β_F and ECS could be constrained.

Another benefit of such a relationship is that it implies that understanding the physics that controls models' variability on the relevant time scales gives insight into the processes that determine models' responses to externally imposed forcings. This would provide an alternative approach to studying these processes, complementing the more commonly used approach of analyzing perturbation experiments.

This is not the first study to analyze the radiation budget of unperturbed simulations of coupled climate models. A number of studies have focused on ''hiatus'' periods, motivated by the recent 15-yr period in which there was an apparent slowdown of global-mean surface temperature increase (e.g., Brown et al. 2014; Xie et al. 2016). A key finding, which agrees with some of the results below, is that there is a phase difference between the internally generated variability of TOA fluxes and the variability of global-mean surface temperature (Xie et al. 2016; Brown et al. 2017).

Other studies have attempted to use models' internal variability and also the variability in observations to estimate the magnitude of the different feedbacks that make up β_F ($\beta_F = \beta_{F,\text{Plank}} + \beta_{F,\text{WV}} + \ldots$). A particular focus has been the cloud feedback. Dessler (2010) estimated this feedback from a combination of reanalysis data and data from the Clouds and the Earth's Radiant Energy System (CERES) experiment for the period 2000–10, during which surface temperature variations were mainly driven by El Niño–Southern Oscillation (ENSO). This produced a positive estimate of the cloud feedback, although the spread was large and encompassed the spread in model cloud feedbacks. It was also found that the cloud feedbacks derived from models' interannual variability are different from the models' long-term cloud feedbacks and this difference was later attributed to different spatial patterns of cloud changes (Dessler 2013). Building on this work, Zhou et al. (2015) compared interannual cloud feedbacks in unforced simulations from the CMIP5 archive with the forced cloud feedbacks in $4\times CO_2$ simulations and found that the interannual feedbacks can explain over 50% of the variance in the forced feedbacks. Interestingly, the spread in the interannual feedbacks is larger than the spread in the forced feedbacks, and again the uncertainty in the estimate of the cloud feedback from CERES spans the range of both sets of feedbacks. Colman and Hanson (2017) found an even better correlation when comparing interannual cloud feedbacks with forced cloud feedbacks in RCP8.5 simulations.

Besides the cloud feedback, Dessler and Wong (2009) estimated the water vapor feedback during ENSO events in models and reanalysis data and found that models generally underestimate this feedback, although there is large uncertainty in the reanalysis estimate. Dalton and Shell (2013) analyzed the unforced Planck feedback, water vapor feedback, and surface albedo feedback in unforced simulations from the CMIP3 archive and found that these were sensitive to the time scale considered, although the estimated values were in rough agreement with the feedbacks in forced experiments. Finally, in addition to the cloud feedback, Colman and Hanson (2017) also found good correlations between the unforced lapse-rate feedback on interannual time scales, the unforced water vapor feedback on decadal time scales, and the unforced surface albedo feedback on interannual time scales and the forced versions of these feedbacks.

These promising results suggest that there is some relation between β_I and β_F. However, these studies have generally focused on models' behavior on specific time scales (seasonal, interannual, decadal, etc.) to estimate the magnitude of the feedbacks. In contrast, we work in

TABLE 1. β_F, ECS, and TCR estimates used in this study and data sources. Here G13 denotes Geoffroy et al. (2013) and F13 denotes Forster et al. (2013). The β_{OLR} and β_{SW} estimates come from Geoffroy et al. (2013) and the TCR, $\beta_{\mathrm{OLR,CS}}$, $\beta_{\mathrm{SW,CS}}$, and β_{CF} estimates come from Forster et al. (2013). CS denotes clear-sky fluxes and CF denotes cloud fluxes. (Expansions of acronyms are available online at http://www.ametsoc.org/PubsAcronymList.)

Model	β_F (F13)/(G13) ($\mathrm{W\,m^{-2}\,K^{-1}}$)	ECS (F13)/(G13) (K)	TCR (K)	β_{OLR} ($\mathrm{W\,m^{-2}\,K^{-1}}$)	β_{SW} ($\mathrm{W\,m^{-2}\,K^{-1}}$)	$\beta_{\mathrm{OLR,CS}}$ ($\mathrm{W\,m^{-2}\,K^{-1}}$)	$\beta_{\mathrm{SW,CS}}$ ($\mathrm{W\,m^{-2}\,K^{-1}}$)	β_{CF} ($\mathrm{W\,m^{-2}\,K^{-1}}$)
BCC-CSM1.1	−1.14/−1.28	2.82/2.9	1.7	−1.69	0.42	−1.91	0.83	−0.07
BNU-ESM	n.a./−0.92	n.a./3.9	n.a.	−1.57	0.65	n.a.	n.a.	n.a
CanESM2	−1.04/−1.06	3.69/3.9	2.4	−1.42	0.37	−1.88	0.71	0.13
CNRM-CM5	−1.14/−1.12	3.25/3.2	2.1	−1.62	0.50	−1.73	0.78	−0.20
CSIRO-Mk3.6.0	0.63/−0.68	4.08/5.1	1.8	−1.97	1.29	−1.70	0.84	0.23
FGOALS-s2	−0.92/−0.87	4.17/4.5	2.4	−1.34	0.47	−1.46	1.02	−0.48
GFDL-CM3	−0.7/n.a.	3.97/n.a.	2.0	n.a.	n.a.	−1.94	0.70	0.48
GFDL-ESM2G	−1.29/n.a.	2.39/n.a.	1.1	n.a.	n.a.	−1.65	0.61	−0.26
GFDL-ESM2M	−1.38/−1.38	2.44/2.5	1.3	−1.37	−0.01	−1.63	0.58	−0.33
GISS-ESM-LR	−1.79/−2.03	2.11/2.25	1.5	−1.48	−0.55	−1.66	0.36	−0.48
HADGEM2-ES	−0.64/−0.61	4.59/5.5	2.5	−1.56	0.96	−1.66	0.65	0.37
INM-CM4	−1.43/−1.56	2.08/1.9	1.3	−2.12	0.55	−1.98	0.67	−0.12
IPSL-CM5A-LR	−0.75/−0.79	4.13/4.25	−2.0	1.92	1.13	−1.99	0.53	0.7
MIROC5	−1.52/−1.58	2.72/2.8	1.5	−1.93	0.35	−1.85	0.84	−0.51
MPI-ESM-LR	−1.13/−1.21	3.63/3.9	2.0	−1.67	0.46	−1.79	0.71	−0.04
MRI-CGCM3	−1.25/−1.31	2.60/2.7	1.6	−2.24	0.93	−1.99	0.83	−0.09
NCAR-CCSM4	−1.23/−1.4	2.89/3.0	1.8	−1.94	0.54	−1.95	0.87	−0.16
NorESM1-M	−1.11/−1.15	2.80/3.25	1.4	−1.82	0.67	−1.86	0.86	−0.11

the frequency domain in order to search for the time scale at which there is the strongest relationship between β_I and β_F. We also do not expect β_I and β_F to have the same magnitude; we are just interested in determining whether their variations are correlated across models. Finally, we have focused more on correlating β_I with the total forced feedback, β_F (and also with the ECS), rather than with the individual feedbacks that make up β_F, although the individual feedbacks are discussed briefly in section 4. In this sense, our study is similar to the recent paper by Cox et al. (2018), although they focused on the variability of surface temperature about long-term historical warming whereas we have studied unforced simulations.

By working in frequency space we can also investigate how the relationships between surface temperature and the TOA fluxes change on different time scales. This provides insight into the time scales and processes that govern models' internal variability. It is also a step toward understanding how models respond to forcings with different frequencies (e.g., MacMynowski et al. 2011), which is a useful way of probing the dynamics that govern models' responses to time-varying forces, and provides context for extrapolating from short-lived climate perturbations, such as volcanic eruptions, to more sustained perturbations, such as increases in greenhouse gas concentrations (Merlis et al. 2014).

The data and methods used in this study are described in the next section. The regression results are presented in section 3 and then the estimates of β_I are compared with β_F and ECS estimates in section 4. A conceptual model for the unforced variability of surface temperature and TOA fluxes is described and compared to data from the CMIP5 archive in section 5. This model provides a physical interpretation for the results of the previous sections. We end with conclusions.

2. Data and methods

The 18 models used in this study are listed in Table 1. Estimates of the models' β_F and ECS values have been published previously by Forster et al. (2013) and Geoffroy et al. (2013), except for the GFDL-CM3 and GFDL-ESM2G models, whose sensitivities were only estimated by Forster et al. (2013), and the BNU-ESM model, whose sensitivities were only estimated by Geoffroy et al. (2013). Both studies estimated the β_F and ECS values from the $4\times CO_2$ experiments in the CMIP5 archive, but Forster et al. (2013) used the Gregory et al. (2004) method to estimate the values, whereas Geoffroy et al. (2013) estimated values as part of their iterative fitting of an energy balance model. The two sets of estimates are highly correlated, with an r^2 value of approximately 0.95. We refer to the Forster et al. (2013) estimates as the $\beta_{F,1}$ and ECS_1 values and the Geoffroy et al. (2013) estimates as the $\beta_{F,2}$ and ECS_2 values. We have also assessed the correlation between our estimates of β_I and estimates of the models' transient climate

responses (TCRs; the response after 70 years to increasing CO_2 concentrations by 1% yr^{-1}) from Forster et al. (2013) and with estimates of some of the individual feedbacks making up β_F (see Table 1).

Data were taken from the preindustrial control (''piControl'') experiments in the CMIP5 archive. For each model 500 simulation years were used in the analysis (for some models more than 500 years are available, in which case only the first 500 years were retained). The variables used in the analysis were the surface air temperature, the TOA outgoing longwave radiation, the TOA outgoing shortwave radiation, the TOA outgoing clear-sky longwave radiation, and the TOA outgoing clear-sky shortwave radiation. The incoming solar radiation was assumed to be fixed. Cloud fluxes were computed as the total flux minus the clear-sky flux. Global and annual means were taken and then the linear trends were subtracted from the time series to remove model drift (although note that some models have nonlinear drift). All the calculations have been repeated using deseasonalized, detrended monthly time series and the results are very similar, although the intermodel spread is somewhat larger. Throughout this paper fluxes are positive when they are out of the TOA.

The spectra of the model variables were estimated using Thomson's multitaper method (Percival and Walden 1993), which is similar to the more commonly used periodogram method for estimating spectral density. In the periodogram method, rectangular windows are applied to the data, the power of each filtered signal is calculated, and the resulting estimates are then averaged together to produce the final estimate of the spectral density. The multitaper method uses a set of optimal windows (tapers), derived from the discrete prolate spheroid sequences, instead of rectangular windows, producing an improved estimate of the spectral density. The number of windows is a free parameter: using more windows reduces the variance of the estimate, but it also produces more spectral leakage. We have found eight windows to produce good estimates for our data, but return to this point in section 4a.

Frequency-dependent regression coefficients, or ''transfer functions'' (MacMartin and Tziperman 2014), can be calculated as

$$\tau(\omega) = \frac{C_{\mathrm{TR}}(\omega)}{P_{\mathrm{TT}}(\omega)}, \tag{3}$$

where ω is frequency, P_{TT} is the power spectrum of global-mean surface temperature for a particular model, and C_{TR} is the cross-spectrum of surface temperature with a particular TOA flux R. However, since τ is complex we consider its amplitude (a) and phase (ϕ) separately:

$$a(\omega) = \frac{|C_{\mathrm{TR}}(\omega)|}{P_{\mathrm{TT}}(\omega)}, \tag{4a}$$

$$\phi(\omega) = \tan^{-1}\left[\frac{\mathrm{Im}\{C_{\mathrm{TR}}(\omega)\}}{\mathrm{Re}\{C_{\mathrm{TR}}(\omega)\}}\right]. \tag{4b}$$

Note that $a \geq 0$ and we will refer to values of a as ''amplitudes'' as a shorthand for ''amplitudes of the transfer functions.'' Also, P_{TT} is always real and positive-definite so it is not necessary to take its absolute value in Eq. (4a). The phase is always between $-180°$ and $180°$, with a phase of $-180°$ being the same as a phase of $180°$, and we take positive phase to mean that the surface temperature leads the TOA flux. To make our figures more legible, we have added $360°$ to any phase value below $-90°$. This minimizes jumps between phases at adjacent frequencies of $-179°$ and $179°$, for instance.

If $\phi(\omega) = 0°$ then $a(\omega) = \beta_I(\omega)$ and an increase in T corresponds to an increase in R, while if $\phi(\omega) = 180°$ then $a(\omega) = -\beta_I(\omega)$ and an increase in T results in a decrease in R. In these two cases β_I can be interpreted as a feedback coefficient. If $\phi(\omega) = \pm 90°$ then one variable is proportional to the derivative of the other, with the sign of the relationship ambiguous. For instance, $dR/dt = -T$ and $dT/dt = R$ will both produce a phase of $+90°$. Physical reasoning must be used to differentiate between these two scenarios, with $a = \omega^{-1}$ and ω in these two cases, respectively.

If the phase is not equal to $0°$, $\pm 90°$, or $180°$ then T and R both have components that are linearly related (and so have a phase of $0°$ or $\pm 180°$) and components that are in quadrature (and so have a phase of $\pm 90°$).

The robustness of the relationships between surface temperature and the TOA fluxes was assessed using the squared coherence:

$$\mathrm{Coh}^2_{\mathrm{TR}}(\omega) = \frac{|C_{\mathrm{TR}}(\omega)|^2}{P_{\mathrm{TT}}(\omega)P_{\mathrm{RR}}(\omega)}. \tag{5}$$

This is similar to a cross-correlation coefficient in frequency and varies between 0 (T and R are completely uncorrelated at a given frequency) and 1 (T and R are perfectly correlated at a given frequency).

3. Regression results

a. Global-mean regressions

The coherence, phase, and amplitudes for surface temperature and the outgoing longwave flux, the outgoing shortwave flux, and the total outgoing TOA flux of the 18 models are shown in Fig. 1. There is significant intermodel spread for all of these quantities but a number of features are still noticeable. Most prominently, there is a difference

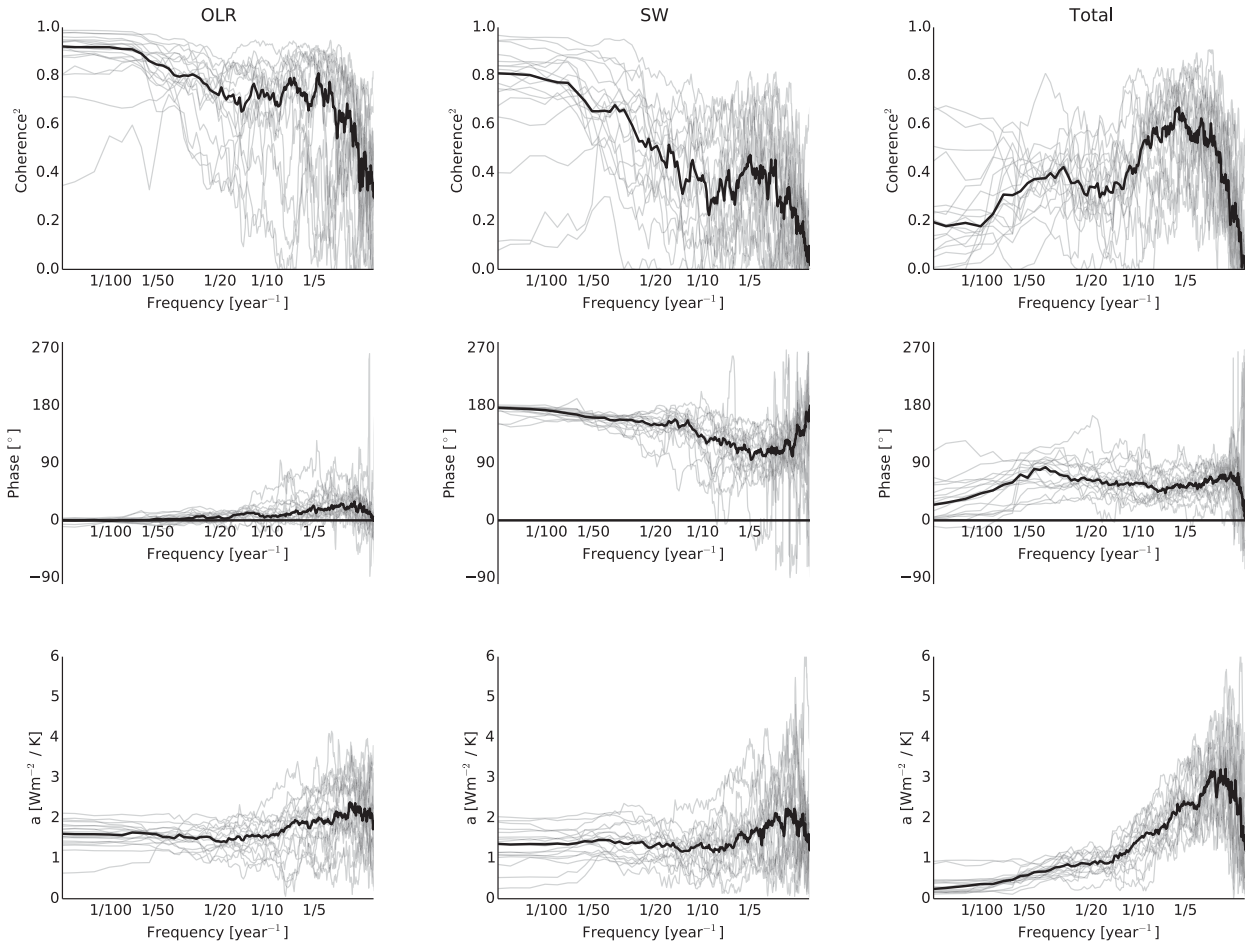

FIG. 1. (top) The (left) squared coherence between global-mean surface temperature and the outgoing longwave flux, (middle) outgoing shortwave flux, and (right) total TOA flux for the CMIP5 models listed in Table 1. The individual models are in gray and the ensemble medians are shown by the thick black lines. Also shown are (middle) the phase relationships between surface temperature and the fluxes and (bottom) the amplitudes. Positive phase means that surface temperature leads the TOA flux, although if two variables are ±90° out of phase then either one variable forces the other or one variable damps the other. For instance, the phase will be +90° if $T = -d\mathrm{SW}/dt$ or if $dT/dt = \mathrm{SW}$. By definition, $a \geq 0$ regardless of the sign of the relationship between two variables.

between the models' behavior on subdecadal ("short") time scales and on longer time scales. This is most clear in the shortwave, which in the median transitions from being about +100° out of phase with the surface temperature at short time scales to almost 180° out of phase on longer time scales. Similarly, there is a local maximum in the coherence at about 1/5 yr^{-1} frequency, then a dip at about 1/10 yr^{-1} frequency, after which the coherence increases again on longer time scales. The maximum value of a is at 1/2.5 yr^{-1} and then a decreases until it is roughly constant for decadal and longer time scales. There is a large spread in the amplitudes at high frequencies.

The longwave is more coherent with surface temperature than the shortwave at all frequencies, but it has the same pattern: there is a maximum at about 1/5 yr^{-1} and then the coherence is large for variability on time scales longer than decadal. The longwave is approximately in phase with the surface temperature at all frequencies, although at high frequencies the phase does increase to about +15° in the ensemble median. The values of a for the longwave are similar to the shortwave values, but they are slightly larger at low frequencies and there is generally less intermodel spread.

These phase relationships indicate that the longwave flux mostly acts as a negative feedback on temperature variability at all time scales. The shortwave flux acts as a positive feedback on temperature variability at long time scales (hence the ~180° phase at low frequencies), whereas on short time scales the ~90° phase difference implies that the shortwave flux either forces surface temperature variations or else is damped by surface temperature variations. As was found by Xie et al. (2016) and

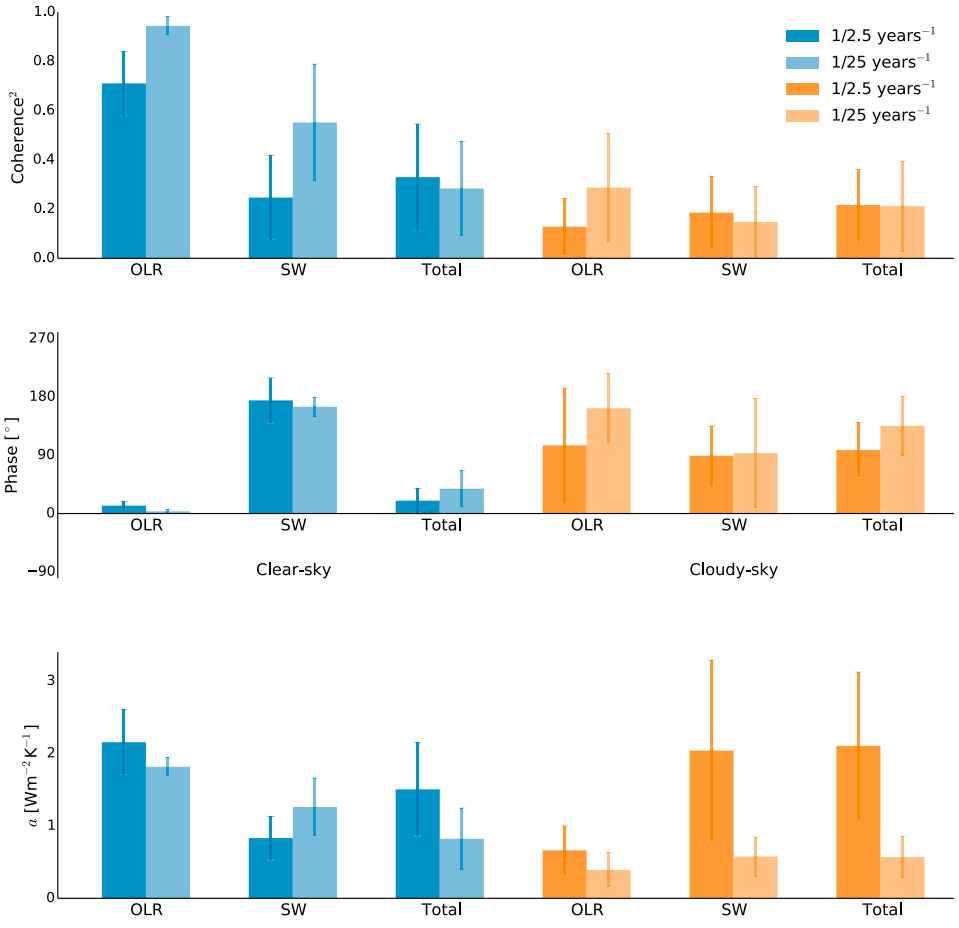

FIG. 2. (top) The ensemble-median squared-coherence between the surface temperature and the outgoing clear-sky (blue bars) and cloudy-sky (orange bars) fluxes at 1/2.5 yr^{-1} (dark bars) and 1/25 yr^{-1} (light bars) frequency. The error bars show plus/minus one standard deviation. Also shown are (middle) the phase relationships at these frequencies and (bottom) the amplitudes. Positive phase means that surface temperature leads the TOA flux and, by definition, $a \geq 0$ regardless of the sign of the relationship between two variables.

Brown et al. (2017), lag regressions reveal that the shortwave leads surface temperature in the models (not shown), which suggests that the shortwave flux is forcing surface temperature variability on short time scales. This relationship is discussed in more detail in section 5, however.

The coherence of the total outgoing TOA flux and the surface temperature also has a maximum at 1/5 yr^{-1} but then decreases and stays roughly constant at 0.3 for variability on time scales between 10 and 50 years, before decreasing again. The coherence at high frequencies is intermediate between the shortwave and longwave coherences. The phase also lies between the shortwave and longwave values, and transitions from about +60° at high frequencies to about +90° on longer time scales, although the intermodel spread is large. The value of a peaks at 1/2.5 yr^{-1} and then decreases monotonically as the frequency decreases.

The low coherence and small amplitudes for the total outgoing flux at low frequencies are the result of a near cancellation between the longwave and shortwave fluxes. These have similar values of a at these frequencies and are almost 180° out of phase with each other, implying that the fluxes are of opposing sign. This results in the total outgoing TOA flux having little variability on long time scales, reflecting the fact that GCMs have a net TOA imbalance close to zero on long time scales. The models do have low-frequency surface temperature variability, however, and so the coherence between the total TOA flux and the surface temperature is weak on long time scales.

b. *Breakdown into clear-sky and cloud components*

To further understand the relationships between the surface temperature and the TOA fluxes, Fig. 2 compares the clear-sky and cloud components of the fluxes. Values

are only shown for frequencies of 1/2.5 yr^{-1} and 1/25 yr^{-1} to aid exposition, but the results are qualitatively insensitive to the choice of frequencies.

The relationship between the all-sky longwave flux and the surface temperature is dominated by the clear-sky component of the flux. This is highly coherent with surface temperature at both frequencies, approaching 1 at lower frequencies, and is also almost exactly in phase with the surface temperature. At low frequencies the value of a for the clear-sky longwave is roughly 1.8 $W m^{-2} K^{-1}$, which is very similar to the clear-sky longwave feedback estimates by Andrews et al. (2012) and by Forster et al. (2013) (i.e., on long time scales $|\beta_{I,\mathrm{CSOLR}}| \approx |\beta_{F,\mathrm{CSOLR}}|$), and there is little intermodel spread. The cloud component of the longwave flux has low (<0.2) coherence with surface temperature at high frequencies but is more coherent at low frequencies. At high frequencies it is about +90° out of phase with surface temperature, although there is a large model spread, and the amplitude is always less than 1 $W m^{-2} K^{-1}$.

The shortwave flux is more complicated. At high frequencies the clear-sky and cloud components are similarly coherent with surface temperature, and the clear-sky flux is approximately 180° out of phase with surface temperature while the cloudy-sky flux is in quadrature with surface temperature. The clear-sky value of a is about 0.7 $W m^{-2} K^{-1}$ and the cloudy-sky value is about 2.2 $W m^{-2} K^{-1}$. In Fig. 1 the total shortwave flux is roughly in quadrature with surface temperature and has a value of a close to 2 $W m^{-2} K^{-1}$ at high frequencies, which suggests that the cloud component mostly determines the shortwave variability at high frequencies. At low frequencies the clear-sky shortwave flux is much more coherent with the surface temperature than the cloudy-sky flux and also has a significantly larger value of a, and so it mostly determines the shortwave variability at low frequencies.

Finally, the clear-sky and cloud components contribute approximately equally to the relationship between the total TOA flux and the surface temperature. At both frequencies, the clear-sky and cloud components have similar coherences with surface temperature, and the amplitudes also have roughly the same magnitude. The cloud component is roughly in quadrature with the surface temperature at both frequencies, while the clear-sky flux has a small positive phase. The center-right panel of Fig. 1 shows that the total TOA flux is 45°–60° out of phase with surface temperature at almost all frequencies, which is intermediate between the phase of the total clear-sky flux and the total cloud flux. This is further evidence that both components contribute roughly equally to the total TOA flux variability.

c. *Breakdown into tropical and extratropical components*

Figure 3 repeats Fig. 2 but now compares the tropical and extratropical variability. That is, the regression analysis is repeated using only the tropical mean temperature (30°S–30°N) and using only the extratropical mean temperature (everywhere else), but still using global-mean TOA fluxes.

There is a transition from the tropical temperatures being more closely related with TOA fluxes on short time scales to the extratropical temperatures being more closely related on long time scales. For instance, the tropical temperatures are generally more coherent with the TOA fluxes on short time scales and the extratropical temperatures are more coherent on longer time scales (although for the OLR the tropical and extratropical coherences are roughly equal at 2.5 yr^{-1}). The values of a are also much larger for the tropical temperature variability at high frequencies than for the extratropical temperature variability. Interestingly, the amplitudes have roughly the same values for both the tropical temperatures and the extratropical temperatures at low frequencies; we have not investigated why this is the case.

The shortwave flux is +90° to +100° out of phase with the tropical surface temperature and +160° to 180° out of phase with the extratropical temperature. The previous section showed that at high frequencies shortwave flux variability is dominated by its cloudy component, which is about +90° out of phase with the global-mean surface temperature, whereas at low frequencies shortwave flux variability is dominated by its clear-sky component, which is about 180° out of phase with global-mean surface temperature. Putting all this together, we conclude that at high frequencies the variability of the shortwave flux is mostly determined by the relationship between clouds and tropical surface temperatures, while at low frequencies the shortwave flux variability is mostly determined by the relationship between extratropical temperatures and the clear-sky shortwave flux. This suggests that changes in sea ice and snow cover largely determine shortwave variability on long time scales.

In contrast, the longwave flux is always dominated by its clear-sky component (previous section), and at high frequencies its variability is mostly driven by tropical temperatures, while at low frequencies its variability is driven by extratropical temperatures. The total TOA flux also transitions from being more related to tropical temperatures at high frequencies to being more related to extratropical temperatures at low frequencies.

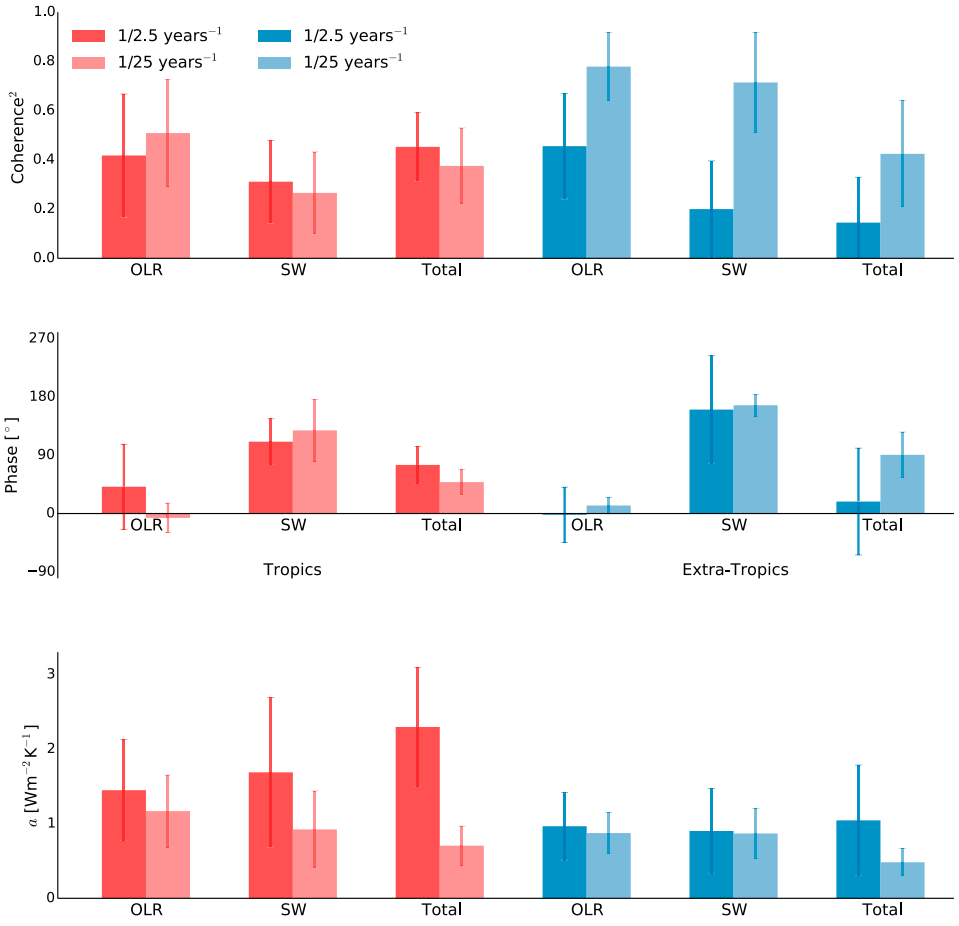

FIG. 3. As in Fig. 2, but for the relationships between the TOA fluxes and tropical mean temperatures (red bars) and extratropical mean temperatures (blue bars). Positive phase means that surface temperature leads the TOA flux; by definition, $a \geq 0$ regardless of the sign of the relationship between two variables.

4. Comparing with sensitivity estimates

a. *ECS and β_F estimates*

Figure 4 shows r^2 values for correlations across the CMIP5 models between the amplitudes at each frequency, $a(\omega)$, for the various TOA flux components and the two sets of β_F and ECS estimates, as well as with the set of TCR estimates. The values of a for the total cloudy-sky flux are most strongly related to the ECS and β_F estimates, particularly at time scales of slightly more than 2.5 years. The amplitudes of the cloudy shortwave flux are also well correlated with the sensitivity estimates, but less than the amplitudes of the total cloudy-sky flux. This implies that adding the cloudy longwave flux improves the relationship, although because of the relatively small sample size this better correlation may not be physical. The correlations are slightly better with the $\beta_{F,2}$ and ECS_2 estimates than with the $\beta_{F,1}$ and ECS_1 estimates, and none of the amplitudes is strongly related to the TCR estimates. We believe that this is because the intermodel spread in TCR is due to variations in the rate of energy exchange between the deep ocean and the mixed layer, in addition to variations in β_F.

Scatterplots of the amplitudes for the total cloudy-sky flux, averaged over the 1/2.5 yr^{-1} to 1/3 yr^{-1} frequency band, versus the $\beta_{F,2}$ (left panel) and ECS_2 (right panel) estimates are shown in Fig. 5. There is a strong relationship with both quantities, as the amplitudes explain roughly 60% of the variance in the models' sensitivities. The amplitudes are negatively correlated with the β_F values and positively correlated with the ECS values: models with larger total cloudy-sky flux amplitudes on these time scales have larger ECS values. The physical interpretation of this relationship is discussed in section 5.

We have used bootstrapping to assess the likelihood of such a strong correlation appearing between two randomly distributed variables over a frequency band of

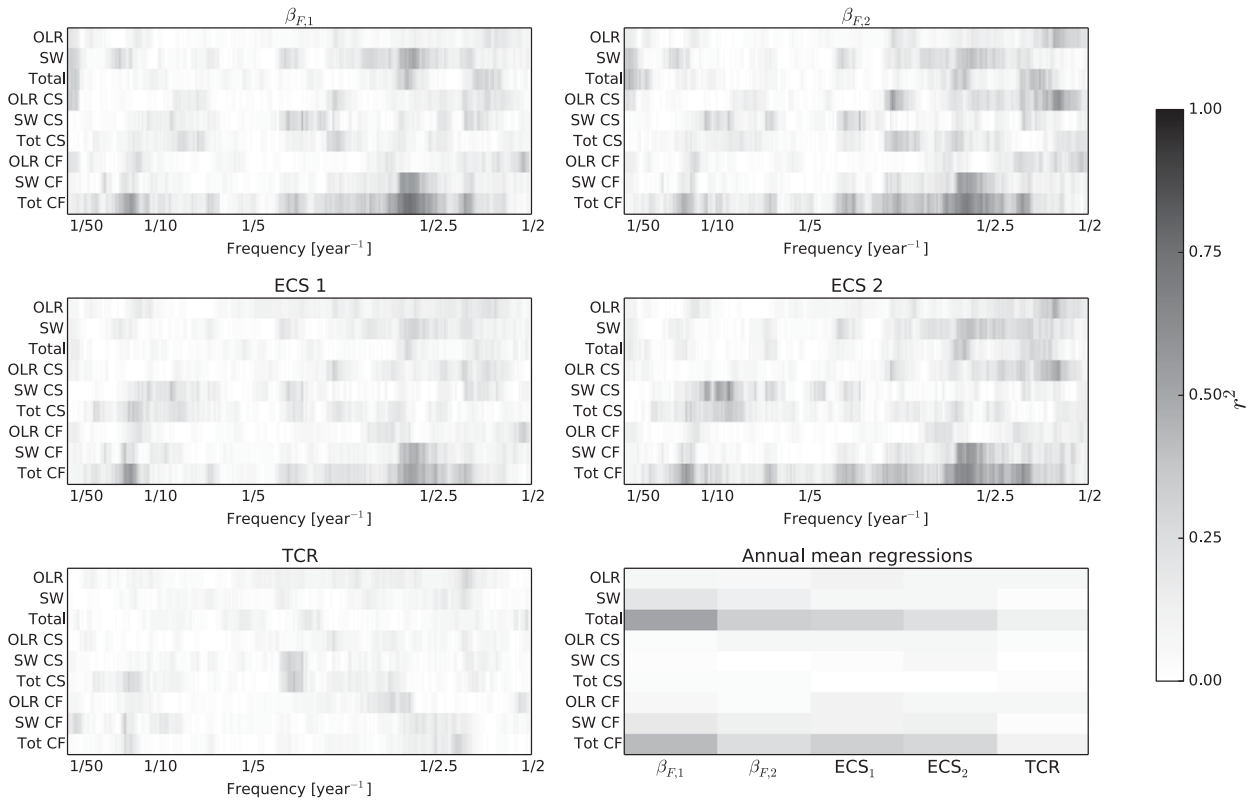

FIG. 4. Shown are r^2 values for correlations between the amplitudes and the two sets of β estimates, the two sets of ECS estimates, and the TCR estimates. Here CS denotes clear-sky fluxes and CF denotes cloud fluxes. The bottom-right panel shows the r^2 values for correlations between the sensitivity estimates and the regression coefficients from regressions between the annual-mean surface temperature and the annual-mean TOA fluxes.

this size. To do this, the total cloudy-sky flux amplitudes were randomly shuffled across the models for each frequency between 1/2.5 yr^{-1} to 1/3 yr^{-1}, then the new amplitudes across this frequency band were averaged for each model and r^2 values were calculated for the correlations between the new set of averaged amplitudes and the estimates of $\beta_{F,2}$. Repeating this procedure one million times indicates a 0.04% probability of the r^2 value being greater than or equal to 0.6 by chance alone.

We have also performed linear regressions between the annual-mean TOA fluxes and the annual-mean surface temperatures (i.e., not in frequency space). We refer to these as the ''annual-mean'' regressions and the bottom right panel of Fig. 4 shows the r^2 values for correlations between the annual-mean regression coefficients and the sensitivity estimates. There are reasonable correlations between the sensitivity estimates and the regression coefficients for the surface temperature and the total TOA flux and the regression coefficients for the surface temperature and the total cloudy-sky flux, with the r^2 values generally around 0.3. There is a particularly strong correlation between the $\beta_{F,1}$ estimates and the coefficients for the total TOA flux, with an r^2 value of about 0.5; however, much of this is due to the GISS-ESM-LR model, which is an outlier. If this point is removed the r^2 drops to ~0.35.

The much lower correlations between the annual-mean regression coefficients and the sensitivity estimates compared with the frequency-dependent regression coefficient on time scales of 2.5–3 years further demonstrates the usefulness of working in frequency space, as we have identified the time scales on which the relationship between T_I and N_I gives the most information about the models' sensitivities to external forcings.

b. *Toward an observational constraint*

That the best correlations are on time scales of 2.5 to 3 years suggests that it may be possible to use these results to develop an observational constraint for Earth's ECS. For instance, the satellite era comprises about 30 years' worth of data, although the longest continuous record of Earth's TOA fluxes (from CERES) only includes 16 years of data.

To assess how accurately the total cloud value of a could be estimated with 30 years' worth of perfect observations, the spectral calculations were repeated

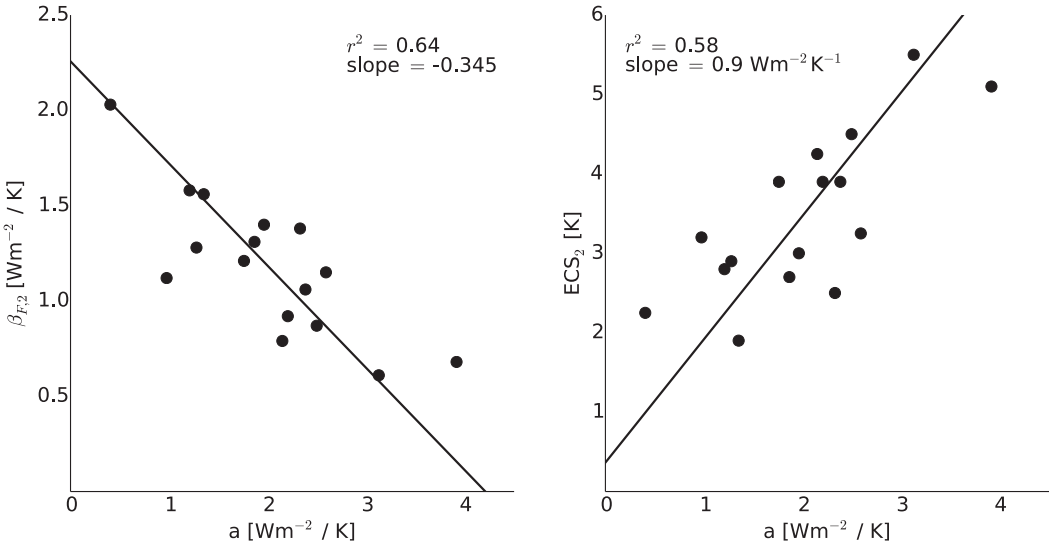

FIG. 5. (left) A scatterplot of the amplitudes for the total cloud flux averaged between 1/3 and 1/2.5 yr^{-1} vs the $\beta_{F,2}$ estimates. The line shows a linear-least squares fit and the r^2 value and slope are in the top-right corner. (right) An analogous plot for the ECS$_2$ estimates.

using every 30-yr segment of the 500 years of simulation from each model. Figure 6 shows probability density functions of the resulting r^2 values and slopes for linear regressions between the new cloud amplitudes and the $\beta_{F,2}$ and ECS$_2$ estimates. From this it can be seen that including fewer years in the calculations degrades the relationship, with the mean r^2 values and the mean slopes less than half those when all the data are used.

It is possible that the filtering used when estimating the spectra overly damps the variance across models when shorter datasets are used (see third paragraph of section 2) and so the calculations were repeated using four spectral windows, rather than eight. This marginally improves the r^2 values, but produces significantly better estimates of the slopes (solid black lines in the bottom row of Fig. 6). So with 30 years' worth of data we would still expect to explain only 25%–30% of the intermodel spread in β_F and ECS. This improves if longer segments are used: with 50 years' worth of data the mean r^2 values are above 0.35, and with 100 years' worth of data the mean r^2 values approach 0.5.

The time scale of 2.5 years is roughly the same as that of the ENSO cycle, suggesting that the total cloud regression coefficients could be estimated from just a few large ENSO events. To test this, the regression coefficients for the total cloudy-sky flux were estimated from the largest ENSO events in the models, with the definition of "large" events ranging from the single largest event to the five largest events. However, no robust relationships were found between these and the sensitivity estimates. This agrees with previous studies showing that accurately estimating the ENSO spectrum requires $O(100)$ years of data (e.g., Wittenberg 2009; Stevenson et al. 2010). Since our method relies on estimating spectra on ENSO time scales, it is not surprising that we need a similar amount of data to produce robust relationships. Other methods of estimating Earth's sensitivity from its internal variability that do not rely on accurately estimating the spectra of surface temperature and the TOA fluxes may converge more quickly (Zhou et al. 2015; Cox et al. 2018).

c. *Individual feedbacks*

Although our focus is on the relationship between β_I and β_F, we have also compared our results with the individual feedbacks making up β_F: in addition to their β_F estimates, Geoffroy et al. (2013) provide estimates of the total longwave and shortwave feedbacks in forced simulations, while Forster et al. (2013) provide estimates of the clear-sky longwave and clear-sky shortwave feedbacks and the total cloud radiative forcing (CRF; Soden et al. 2004).

The left panel of Fig. 7 shows the median amplitudes as a function of frequency for these different components as well as the two standard deviation ranges of the absolute values of the estimates of the corresponding forced feedbacks (arrows to left of panel; note that the CRF can be positive or negative). At high frequencies the amplitudes are generally larger than the forced feedbacks, except for the clear-sky shortwave, which is close to its forced value on subdecadal time scales. On longer time scales the clear-sky longwave and total

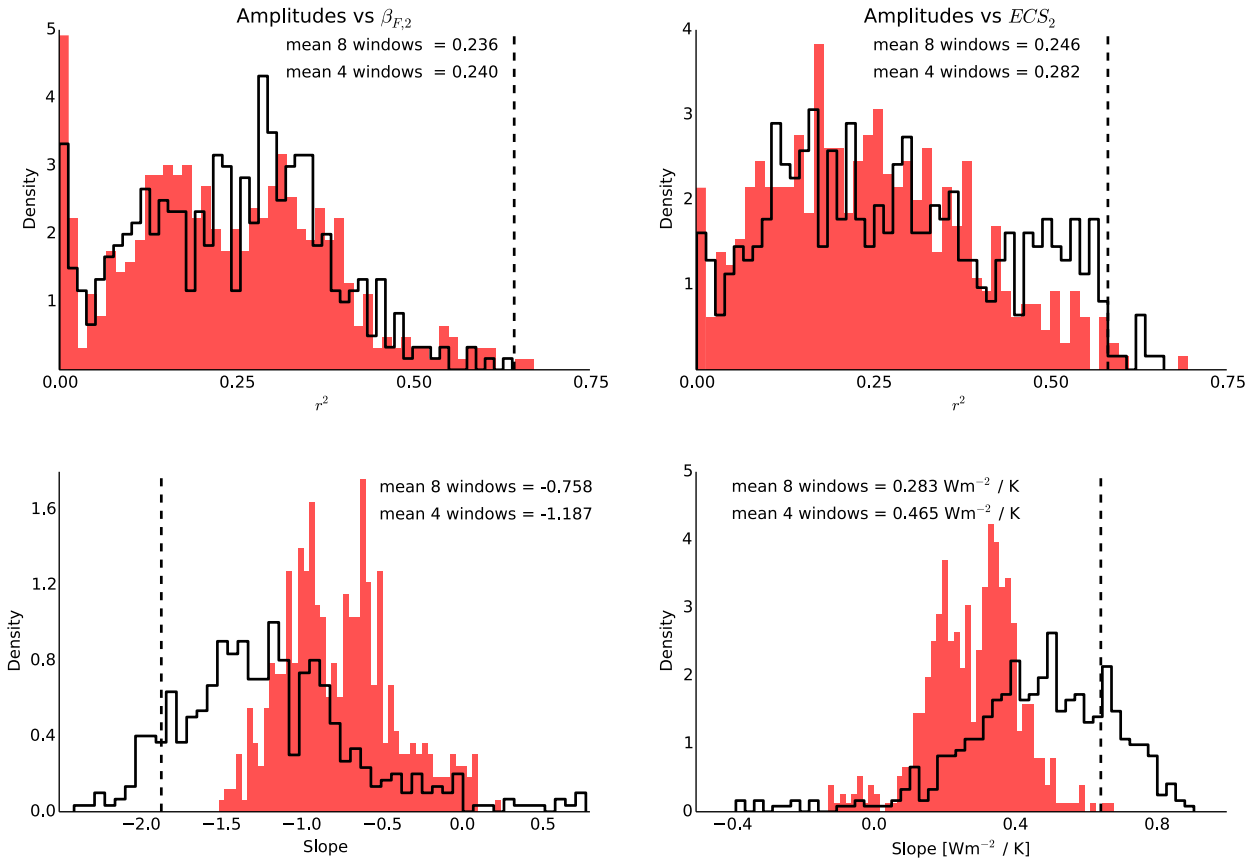

FIG. 6. (top left) The probability density functions (PDFs) of r^2 values for correlations between the $\beta_{F,2}$ estimates and the amplitudes for the total cloud flux averaged between 1/3 and 1/2.5 yr^{-1}, with the latter calculated using every 30-yr segment in the 500 years of simulation for each model. The red bars show the PDFs when eight spectral windows are used to estimate the spectra while the black lines show the estimates when four windows are used. The dashed vertical black line marks the r^2 value when the calculations are performed with all 500 years of data. Other panels are similar, but for (top right) the ECS_2 estimates, (bottom left) the slopes of the correlations between the $\beta_{F,2}$ estimates and the amplitudes, and (bottom right) the slopes of the correlations between the ECS_2 estimates and the amplitudes.

longwave amplitudes are close to the absolute values of the corresponding forced feedbacks but the shortwave and clear-sky shortwave amplitudes are much larger than their corresponding forced feedbacks, suggesting that changes in snow cover and sea ice feed back more strongly on internally generated temperature variations than on forced temperature perturbations. The total cloud amplitude peaks at about 1/2.5 yr^{-1} frequency and then decreases on longer time scales, and there is large spread in the CRF, so it is unclear whether the two have similar values.

The right panel of Fig. 7 shows the r^2 values for correlations across models between the amplitudes and the forced feedbacks. The strongest relationship ($r^2 > 0.6$) is for the relationship between the CRF and the amplitude of the total cloudy-sky flux at about 1/2.6 yr^{-1}. This is expected from our earlier results (Fig. 4): clouds are responsible for much of the spread in models' β_F and ECS and so if the value of a for the total cloudy-sky flux at this time scale is correlated with β_F we would expect it to also be correlated with the total CRF. There are also reasonable correlations (r^2 of about 0.4) between the amplitudes and the forced feedbacks for the total shortwave flux, both clear-sky fluxes, and the CRF on time scales of 10 to 20 years. These time scales are long enough that the variability is independent of ENSO variations and there is also relatively high coherence between the fluxes and the surface temperature, but the amplitude estimates also have less sampling error than the estimates at lower frequencies.

5. Interpretation with a conceptual model

a. *Fitting the power spectrum of global-mean surface temperature*

To develop a conceptual model for the relationship between surface temperature and the TOA fluxes we begin by fitting the power spectrum of global-mean

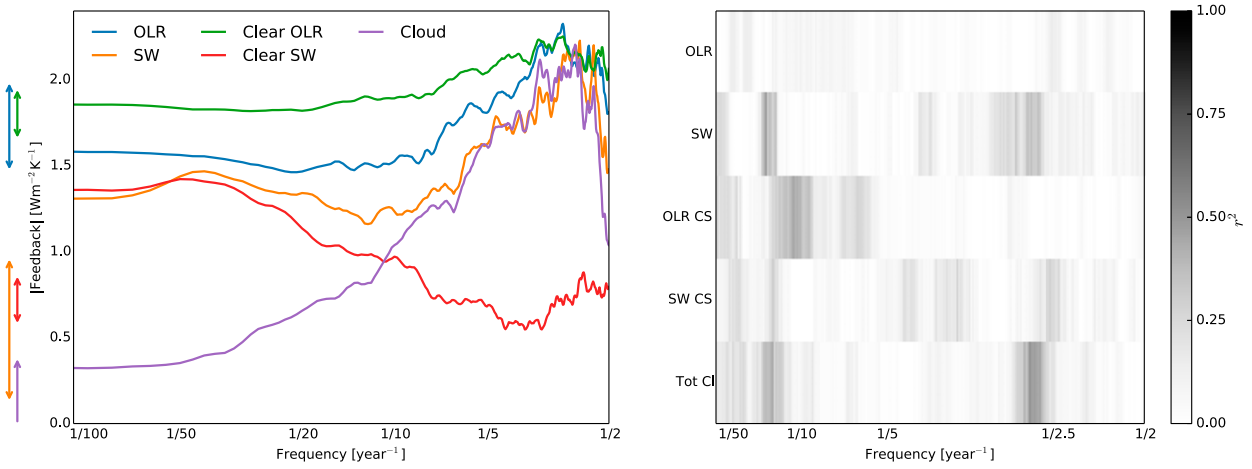

FIG. 7. (left) The ensemble-median amplitudes of various feedbacks as a function of frequency. The arrows to the left of the panel show the two standard deviation ranges of the absolute values of the estimates of the corresponding forced feedbacks from Geoffroy et al. (2013) and Forster et al. (2013) (note that the cloud feedback can be positive or negative). (right) The r^2 values for correlations between the amplitudes of the feedbacks and the estimates of the forced feedbacks.

surface temperature. A natural starting point is the stochastic linear feedback model of Hasselmann (1976) for the temperature variability of the mixed layer (see also Wu and North 2002; Cox et al. 2018):

$$c\frac{dT}{dt} = \beta T + \eta, \tag{6}$$

where T is the mixed-layer temperature, c is the heat capacity of the mixed layer, β is a feedback coefficient, and η is a white noise term. The equation for the power spectrum of this model is given in the appendix.

To fit this system to the ensemble median power spectrum of T the Metropolis version of the Markov chain Monte Carlo (MCMC) method was used to estimate the parameters (Robert and Casella 2004). This is a Bayesian technique for estimating the parameters (θ) of a model for a dataset x, in which a prior probability distribution for the parameters [$P(\theta)$] and the data x are combined to generate a Markov chain that has the posterior distribution [$P(\theta|x)$] as its equilibrium distribution.

Gaussian priors were assumed and, because of the lack of a priori information, the means of the prior distributions were estimated by eye and for each variable the standard deviation was taken to be 10% of the mean. The value of c strongly influences the results of the calculation and the mean of its prior distribution was taken to be 30 W m^{-2} K^{-1} yr^{-1}, which corresponds to a mixed layer depth of about 250 m. This is somewhat deeper than the values used in previous box model fits to coupled model simulations (e.g., Wu and North 2002; Held et al. 2010; Murphy and Forster 2010) but was found to produce a better fit to the spectra. The final parameter values from the MCMC simulations are listed in the second column of Table 2.

The model produces a good fit to the ensemble-median power spectrum at low frequencies ($\leq$1/20 yr^{-1}; Fig. 8), but the power is underestimated at high frequencies. To address this, an ENSO term was added to the right-hand side of Eq. (6):

$$c\frac{dT}{dt} = \beta T + \eta + \gamma \mathrm{ENSO}, \tag{7}$$

where γ is a constant of proportionality with units of W m^{-2} and ENSO is a nondimensional ENSO index. The ENSO index was modeled by white noise filtered using a third-order Butterworth filter to only retain power between 1/8 yr^{-1} and 1/2.2 yr^{-1}, and is shown in the left panel of Fig. 9. This form was again estimated by eye; individual models tend to have a stronger ENSO peak but because we are comparing with the ensemble median the peak is spread out over a broad range of frequencies. The equation for the power spectrum of this system is also given in the appendix and the parameters were again estimated with the MCMC algorithm. The dashed red line in Fig. 8 shows that this additional term results in a much better fit to the power spectrum.

b. *Modeling the relationship between temperature and the TOA fluxes*

The energy balance of the mixed layer can be written as

$$c\frac{dT}{dt} = -N - S,$$

TABLE 2. Parameters estimated by the MCMC algorithm in section 5.

	Hasselmann (1976) model	Model with ENSO term	Constant β_{SW}	Frequency-dependent β_{SW}
c(W m^{-2} K^{-1} yr^{-1})	29.8	31.2	34.6	38.9
β(W m^{-2} K^{-1})	−1.1	−1.05	n.a.	n.a.
σ^2(W m^{-2})	0.049	0.049	n.a.	n.a.
γ(W m^{-2})	n.a.	0.91	n.a.	n.a.
β_{OLR}(W m^{-2} K^{-1})	n.a.	n.a.	−1.80	−1.91
β_{SW}(W m^{-2} K^{-1})	n.a.	n.a.	0.79	0.82
β_S(W m^{-2} K^{-1})	n.a.	n.a.	−0.05	−0.07
σ^2_{OLR}(W m^{-2})	n.a.	n.a.	0.01	0.02
σ^2_{SW}(W m^{-2})	n.a.	n.a.	0.02	0.04
σ^2_S(W m^{-2})	n.a.	n.a.	0.05	0.06
γ_{OLR}(W m^{-2})	n.a.	n.a.	0.0003	0.006
γ_{SW}(W m^{-2})	n.a.	n.a.	0.06	0.09
γ_S(W m^{-2})	n.a.	n.a.	0.62	0.62

where N is the net TOA energy flux and S is the energy flux from the deep ocean into the mixed layer. Assuming that the incoming solar radiation is fixed, then N is the sum of the outgoing longwave and outgoing shortwave radiation (OLR and SW, respectively):

$$c\frac{dT}{dt} = -(\mathrm{OLR} + \mathrm{SW}) - S. \tag{8}$$

Comparing with Eq. (7), each term on the right-hand side of Eq. (8) can be modeled as the sum of a term that is linearly proportional to T, a white-noise term and a term proportional to ENSO:

$$\mathrm{OLR}(t) = -\beta_{\mathrm{OLR}}T(t) - \eta_{\mathrm{OLR}}(t) - \gamma_{\mathrm{OLR}}\mathrm{ENSO}(t), \tag{9a}$$

$$\mathrm{SW}(t) = -\beta_{\mathrm{SW}}T(t) - \eta_{\mathrm{SW}}(t) - \gamma_{SW}\mathrm{ENSO}(t), \tag{9b}$$

$$S(t) = -\beta_S T(t) - \eta_S(t) - \gamma_S\mathrm{ENSO}(t). \tag{9c}$$

Based on the regression analysis in section 3, we interpret the equations for the longwave and shortwave fluxes as follows. The β terms are the clear-sky feedbacks, representing a combination of the Planck feedback, the longwave water vapor feedback, and the lapse-rate feedback for the longwave and a combination of the ice-albedo feedback and the shortwave water vapor feedback for the shortwave. As was shown in section 3b, for both fluxes the clear-sky component dominates the variability on long time scales, when the fluxes act as linear feedbacks on temperature variability.

The ENSO terms represent the effects of ENSO-induced changes in cloud radiation on global-mean surface temperature. The regression analysis showed that tropical clouds dominate the shortwave variability at high frequencies (Fig. 3), when they appear to force temperature variability, and we assume that tropical clouds also play a minor role in the longwave variability at these frequencies. However, although we have not demonstrated it here, we believe that tropical clouds are actually responding to local sea surface temperature (SST) perturbations during ENSO events. Observational and modeling studies have shown that clouds respond quickly to SST perturbations in the tropical Pacific, whereas the global-mean temperature response to these perturbations lags by several months (Klein et al. 1999; Lau and Nath 2001; Zhou et al. 2017; Andrews and Webb 2018). So, from a global-mean perspective, clouds, and hence the SW flux, appear to force surface temperature variability on ENSO time scales when in fact they are responding to warming/cooling of the tropical Pacific and then amplifying the global-mean surface temperature response to the ENSO events.

The S term combines the transfer of heat from the deep ocean to the mixed layer, in the first two terms, with the reorganization of heat between the subsurface and the surface in the tropical Pacific and between the tropical Pacific and the mixed layer over the rest of the world during ENSO events in the third term. The

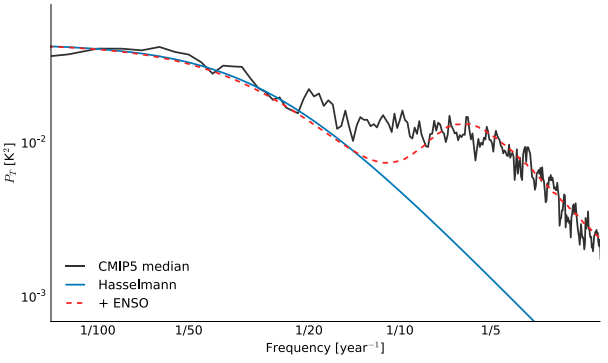

FIG. 8. Ensemble median power spectrum of global-mean surface temperature T in black. The blue line shows the MCMC-derived fit using the Hasselmann (1976) model and the dashed red line shows the MCMC-derived fit using the modified model with the ENSO term.

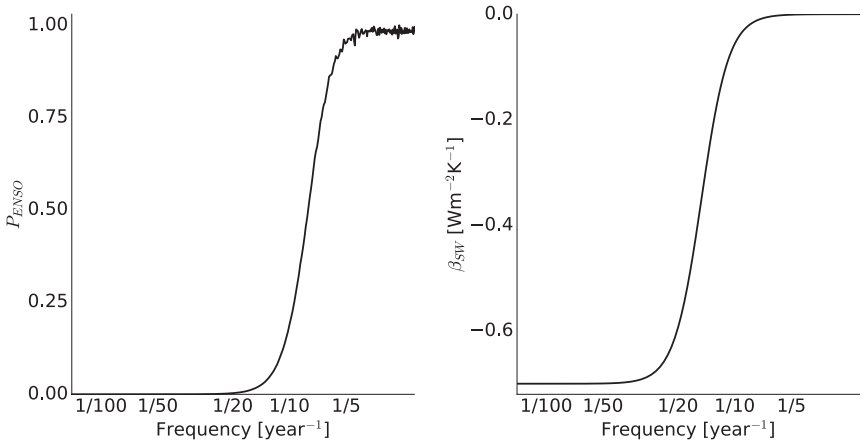

FIG. 9. (left) The power spectrum of ENSO, P_{ENSO}, used in the conceptual model and (right) the frequency-dependent β_{SW}.

equations for the resulting spectra are given in the appendix.

The MCMC algorithm was again used to fit the spectra of the fluxes, testing against the coherence between T and the OLR. Similar estimates were obtained using the coherence between T and SW. There are 10 free parameters in this system; however, several constraints can be placed on their values. When possible, the means of the prior distributions required by the MCMC algorithm were taken from the results of the spectral calculations in section 3. The results of the previous section also constrain the parameters, as we sought to keep $\beta_{\mathrm{OLR}} + \beta_{\mathrm{SW}} + \beta_S \sim \beta$, for instance. However, it was found that a slightly deeper effective mixed-layer depth (closer to 300 m) produced the best fits to the spectra. For each variable the standard deviation was taken to be 10% of the mean. The final parameter values from the MCMC simulations are listed in the fourth column of Table 2.

The phase relations, coherence, and amplitudes produced by the final parameter settings are shown by the blue lines in Fig. 10. The conceptual model does a reasonable job of reproducing these, with the phase relationships particularly well captured. However, the SW coherence is significantly overestimated at almost all frequencies. This can be improved by making β_{SW} frequency dependent, so that it only acts on long time scales. We do not have a rigorous justification for this modification, but this could represent the large thermal inertia of the high-latitude oceans that are responsible for the sea ice variations that drive the ice-albedo feedback. We have modeled β_{SW} as decaying to zero on frequencies higher than 1/15 yr^{-1}, using a second-order Butterworth filter (right panel of Fig. 9). As the dashed red lines in Fig. 10 show, this successfully reduces the coherence between the SW and T, while maintaining the qualitative agreement in the other quantities. The new parameters estimated by the MCMC algorithm are similar to the constant β_{SW} case and are listed in the fifth column of Table 2.

As an aside, taking the forcing to be the ensemble-mean value from Forster et al. (2013) (−3.44 W m^{-2}), the constant β_{SW} version of the conceptual model has an ECS of 3.3 K, which is approximately the ensemble-mean ECS of the CMIP5 models used in this study (Forster et al. 2013; Geoffroy et al. 2013). The frequency-dependent β_{SW} version of the model has a slightly smaller ECS of 3.1 K.

c. Discussion

Both formulations of the conceptual model are able to reproduce the transition of the shortwave from being roughly in quadrature with surface temperature at high frequencies to being 180° out of phase at low frequencies. As can be seen from the final parameter values in Table 2, this is because in both formulations the linear feedback coefficient for the shortwave is relatively small and so the ENSO term dominates the shortwave variability at high frequencies. In contrast, the longwave has a much larger feedback coefficient and so it always acts primarily as a negative feedback on temperature variability, although the ENSO term does result in a small positive phase difference at high frequencies, as was seen in the regressions.

We emphasize, however, that our model is intended to be qualitative, and the final parameter values should not be taken as being physically accurate. Furthermore, our use of a frequency-dependent form for β_{SW} is speculative, and is mostly an ad hoc correction for the model's overestimation of the coherence between SW and T at high frequencies, which does not affect the values of a or

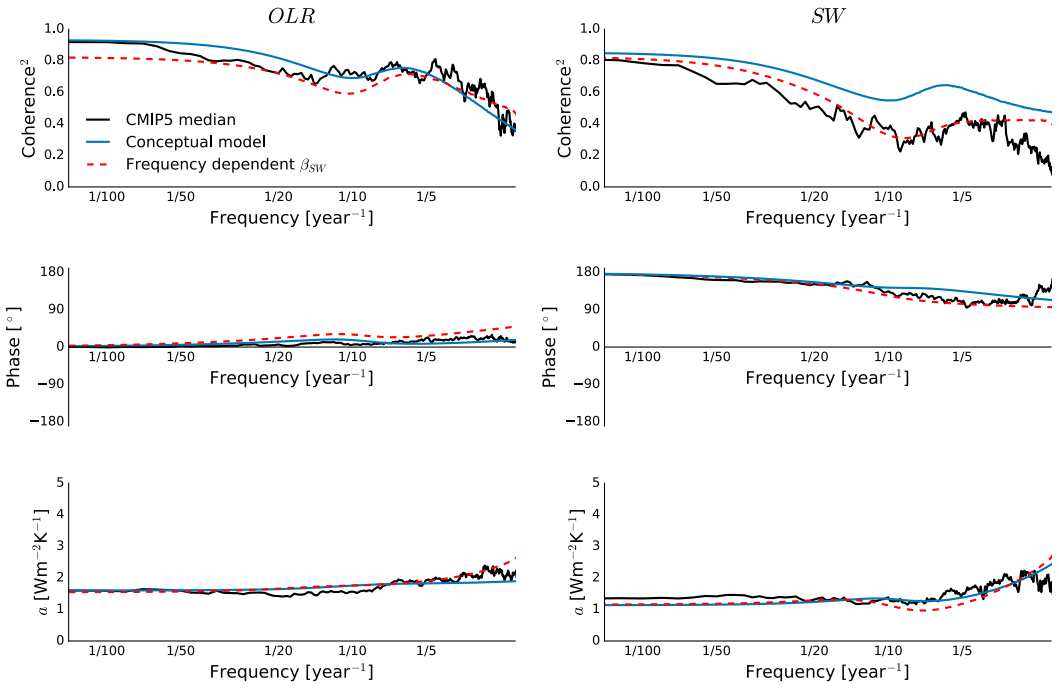

FIG. 10. (left) The (top) ensemble-median coherence, (middle) phase, and (bottom) a for OLR and T in black compared with the results of the conceptual model in blue (constant β_{SW}) and red (frequency-dependent β_{SW}). (right) As at left, but for SW.

of the phase relation between these variables. This frequency dependence could reflect a frequency dependence of sea ice variability due to the thermal inertia of the high-latitude oceans, but we have not attempted to demonstrate that here.

Finally, although they are important for determining the relationship between temperature variability and the radiative fluxes, both γ_{SW} and γ_{OLR} are much smaller than γ_S. This agrees with the finding of Chiang and Sobel (2002) that the global warming associated with El Niño is mostly mediated by surface energy fluxes, rather than TOA fluxes. The values in Table 2 also suggest that the deep ocean does not feed back strongly onto temperature variations (β_S is small compared to β_{OLR} and β_{SW}), which reflects the fact that ocean heat uptake is dominated by the formation of deep North Atlantic and Antarctic bottom waters. As a result, Eq. (8) can be approximated as

$$c\frac{dT}{dt} \approx (\beta_{\mathrm{OLR}} + \beta_{\mathrm{SW}})T + \gamma_S \mathrm{ENSO} + \eta, \qquad (10)$$

where η is the sum of the noise terms.

6. Conclusions

In this study we have investigated whether the internal variability of a subset of the coupled climate models participating in CMIP5 can give insight into the models' sensitivity to external forcings. We have done this by comparing β_I, the coefficient relating the N_I anomalies and T_I anomalies at a given frequency, with β_F, the radiative restoring coefficient of forced temperature perturbations, and ECS, the models' equilibrium climate sensitivity, across the models. By necessity, this has involved working in the frequency domain and so we have also studied the spectral relationships between the TOA fluxes and global-mean surface temperature.

The longwave flux and the surface temperature are generally highly coherent and in phase with each other, as the longwave primarily acts as a negative feedback on surface temperature variability. The relationship between the longwave and the surface temperature is dominated by the clear-sky component of the longwave, with the tropical flux mostly determining the high-frequency variability and the extratropical flux mostly determining the low-frequency variability. On decadal and longer time scales the ensemble-median magnitude of $\beta_{I,\mathrm{CS,OLR}}$ is about 1.8 $\mathrm{W\,m^{-2}\,K^{-1}}$, which agrees with the magnitudes of the estimates of the forced clear-sky longwave feedback by Andrews et al. (2012) and Forster et al. (2013).

The shortwave flux behaves differently at high (shorter than decadal) and low frequencies. At high frequencies it is roughly 90° out of phase with the surface

temperature and its variability is mostly determined by tropical clouds. This suggests that the shortwave flux forces temperature variability at these frequencies, although we believe that the shortwave variability on these time scales is actually due to tropical clouds responding to warming or cooling of the tropical Pacific during ENSO events. These cloud responses amplify the global-mean surface temperature response to these ENSO events, which lags by several months, and so the shortwave flux appears to force the surface temperature when in fact its variability is due to ENSO-induced changes in cloud cover. Future work is needed to verify this interpretation.

At lower frequencies the shortwave and the surface temperature are more coherent and are 180° out of phase, so that the shortwave acts as a positive feedback on surface temperature variability. The shortwave variability on these time scales is mostly determined by the extratropical clear-sky flux, which likely represents sea ice and snow cover variability. The amplitude of the shortwave flux is larger at high frequencies and asymptotes to a value of about 1.6 $\mathrm{W\,m^{-2}\,K^{-1}}$ at low frequencies. At these frequencies the longwave flux and the shortwave flux nearly cancel and so the total TOA flux has little power, a consequence of the models having zero net flux at TOA when averaged over a few decades. At higher frequencies the behavior of the total TOA flux is generally between that of the longwave and the shortwave.

We have found that the total cloud flux amplitudes on time scales of about 2.5 years are well correlated with the β_F and ECS estimates, and can explain up to 60% of the variance across models. This is similar to the correlations between the interannual cloud feedback and the forced cloud feedback found by Zhou et al. (2015) and by Colman and Hanson (2017), although the latter study compared feedbacks derived from RCP8.5 simulations, rather than abrupt $4\times CO_2$ simulations. We emphasize, however, that we have directly compared the feedbacks with the total feedback β_F and the models' ECS, rather than with the individual components of β_F. Another difference is that both studies used the kernel method to estimate the forced cloud feedback (Soden et al. 2008), whereas the estimates of the forced feedbacks used here were obtained using the Gregory et al. (2004) method [the Forster et al. (2013) estimates] and as part of the iterative fitting of a two-box energy balance model [the Geoffroy et al. (2013) estimates].

Figure 5 demonstrates that models with larger total cloudy-sky flux amplitudes generally have larger ECS values. We have suggested that the total cloudy-sky flux amplitudes (which are dominated by the shortwave component) represent the ability of ENSO-induced cloud changes to amplify ENSO-induced surface temperature variations via the tropical atmospheric bridge mechanism described by Klein et al. (1999). From this perspective, the relationship between the amplitudes and the ECS estimates indicates that models in which clouds amplify ENSO-induced surface temperature changes more strongly are also more sensitive to external forcings.

Studying cloud variability on ENSO time scales can thus tell us about Earth's climate sensitivity, even though the patterns of SST variations differ from the forced patterns. A number of recent studies have shown that cloud feedbacks are highly sensitive to the pattern of surface temperature change (Andrews et al. 2015; Zhou et al. 2017; Andrews and Webb 2018), in particular whether the warming is focused in regions of mean ascent or in regions of mean subsidence (or in the extratropics). On interannual to decadal time scales, temperature variability in the preindustrial control simulations is dominated in the tropics by warming/cooling of the central and eastern equatorial Pacific and off the west coast of South America (Fig. 11). Warming of these regions also dominates models' tropical responses to CO_2 perturbations on intermediate and longer time scales, that is, a decade or so after the perturbation is initially applied [e.g., Fig. 7 of Held et al. (2010), center-left panel of Fig. 5 of Andrews et al. (2015), and supplementary Fig. 6 of Proistosescu and Huybers (2017)], which is further suggestive of a link between cloud variability on ENSO time scales and cloud changes in forced experiments.

We have also found that long datasets are required to accurately estimate β_I (Fig. 6). When 30 years are used in the calculations the average r^2 values between the amplitudes and the sensitivity estimates are only 0.25–0.3. Moreover, the slope of the relationship is typically underestimated, although we have shown that the slope can be improved by using fewer windows to estimate the spectra. Another difficulty with using observations is that the forced component must be removed, whereas here we have used unforced simulations.

We conclude that there is a meaningful relationship between β_I and the sensitivity of CMIP5 models, although the models suggest that this relationship is of limited observational use at present, as longer time series of TOA fluxes are required to accurately constrain the relevant β_I values. A caveat to this is that our results depend on the accuracy and diversity of the models' ENSO simulations. AMIP simulations, in which sea surface temperatures are prescribed and so could more realistically mimic Earth's ENSO variability, might provide a more realistic assessment of

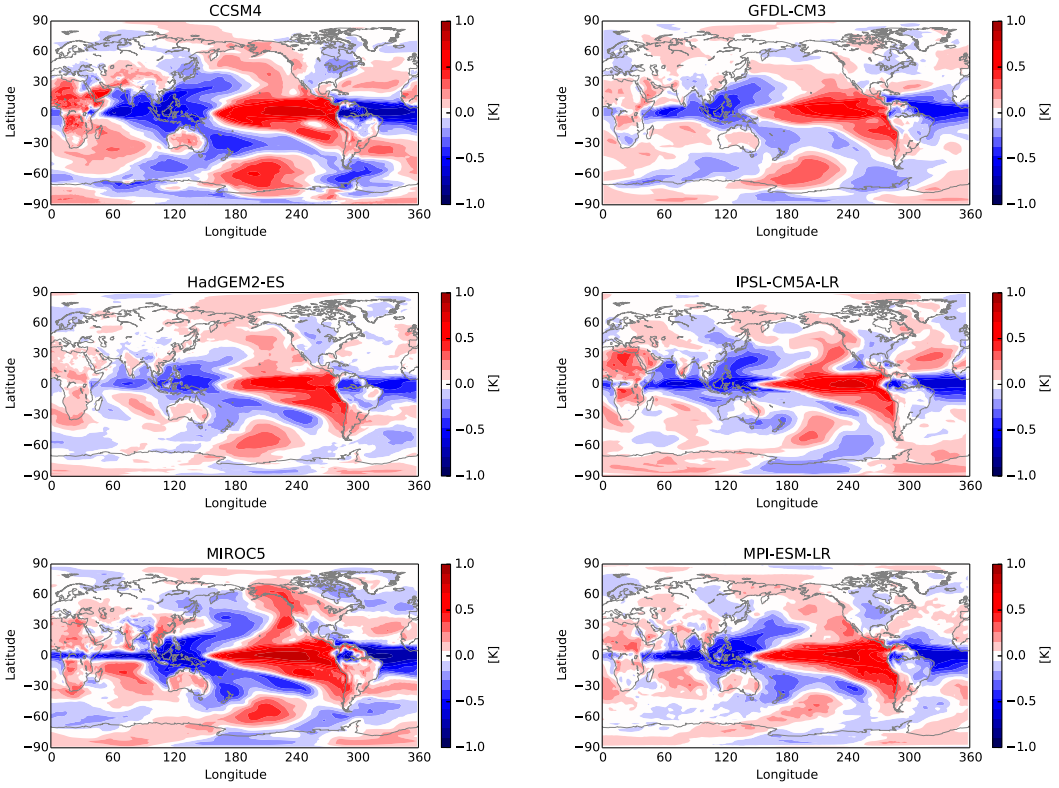

FIG. 11. Lag regressions of deseasonalized and detrended surface temperature regressed and global-mean surface temperature that is bandpass filtered to only retain power at frequencies between 1/2 yr^{-1} and 1/8 yr^{-1}, from the preindustrial control simulations for six of the CMIP5 models used in this study. Global-mean surface temperatures lag by 6 months, corresponding to a 90° phase lag on time scales of 2.5 yr.

the relationship between β_I and climate sensitivity. Nevertheless, our results also point to a novel way of studying the processes determining the intermodel spread of equilibrium climate sensitivity. Previous studies have investigated the relationship between clouds and ENSO (e.g., Klein et al. 1999; Chiang and Sobel 2002; Sun et al. 2006; Lloyd et al. 2012; Radel et al. 2016), and the ability of ENSO-induced cloud cover changes to amplify ENSO-induced surface temperature variations is worth continued study.

Acknowledgments. This project benefited from much guidance and advice from Isaac Held. We thank three anonymous reviewers and the editor, Dr. Steven Klein, for thorough readings and comments, which improved the manuscript significantly. Yi Ming and David Paynter provided comments on an earlier version of this manuscript, and our analysis benefited from helpful discussions with Peter Huybers, Cristian Proistosescu, and Max Popp. Python code for the multitaper spectral analysis is available at http://nicklutsko.github.io/code/. Nicholas Lutsko was supported by NSF Grants DGE 1148900 and AGS 1623218.

APPENDIX

Equations for the Spectra

The power spectrum of temperature in the Hasselmann (1976) model is

$$P_T = \frac{\sigma^2}{\omega^2 c^2 + \beta^2}, \tag{A1}$$

where ω is frequency and σ^2 is the power of the white noise. This is modified by the addition of the ENSO term to

$$P_T = \frac{\sigma^2 + \gamma^2 P_{\mathrm{ENSO}}}{\omega^2 c^2 + \beta^2}, \tag{A2}$$

with P_{ENSO} being the power of the ENSO spectrum (shown in the left panel of Fig. 9).

In the model described in section 5b T can be written in frequency space as

$$\hat{T} = \frac{(\gamma_{\mathrm{OLR}} + \gamma_{\mathrm{SW}} + \gamma_S)\widehat{\mathrm{ENSO}} + \hat{\eta}_{\mathrm{OLR}} + \hat{\eta}_{\mathrm{SW}} + \hat{\eta}_S}{i\omega c_p - \beta_{\mathrm{OLR}} - \beta_{\mathrm{SW}} - \beta_S}, \tag{A3}$$

where circumflexes indicate Fourier transforms. Writing $D = i\omega c - \beta_{\rm OLR} - \beta_{\rm SW} - \beta_S$, the power spectrum of T is then

$$P_T(\omega) = \langle \hat{T}\hat{T}^* \rangle = \frac{(\gamma_{\rm OLR} + \gamma_{\rm SW} + \gamma_S)^2 P_{\rm ENSO} + \sigma_{\rm OLR}^2 + \sigma_{\rm SW}^2 + \sigma_S^2}{\langle DD^* \rangle}. \tag{A4}$$

The equation for the OLR can be written as

$$\widehat{\rm OLR} = -\beta_{\rm OLR} \frac{(\gamma_{\rm SW} + \gamma_S)\widehat{\rm ENSO} + \hat{\eta}_{\rm SW} + \hat{\eta}_S}{D} - \frac{(\hat{\eta}_{\rm OLR} + \gamma_{\rm OLR}\widehat{\rm ENSO})(i\omega c - \beta_{\rm SW} - \beta_S)}{D},$$

and hence its spectrum is

$$P_{\rm OLR} = \frac{\beta_{\rm OLR}^2}{\langle DD^* \rangle}[(\gamma_{\rm SW} + \gamma_S)^2 P_{\rm ENSO} + \sigma_{\rm SW}^2 + \sigma_S^2] + \frac{\sigma_{\rm OLR}^2 + \gamma_{\rm OLR}^2 P_{\rm ENSO}}{\langle DD^* \rangle}[\omega^2 c^2 - (\beta_{\rm SW} + \beta_S)^2]. \tag{A5}$$

Analogously for SW,

$$P_{\rm SW} = \frac{\beta_{\rm SW}^2}{\langle DD^* \rangle}[(\gamma_{\rm OLR} + \gamma_S)^2 P_{\rm ENSO} + \sigma_{\rm OLR}^2 + \sigma_S^2] + \frac{\sigma_{\rm SW}^2 + \gamma_{\rm SW}^2 P_{\rm ENSO}}{\langle DD^* \rangle}[\omega^2 c^2 - (\beta_{\rm OLR} + \beta_S)^2]. \tag{A6}$$

Finally, the cross-spectra are given by

$$C_{{\rm OLR},T} = \langle \widehat{\rm OLR}\hat{T}^* \rangle = -\beta_{\rm OLR} P_T(\omega) - \frac{\sigma_{\rm OLR}^2 + \gamma_{\rm OLR}(\gamma_{\rm OLR} + \gamma_{\rm SW} + c_S)P_{\rm ENSO}}{D^*}, \tag{A7a}$$

$$C_{{\rm SW},T} = \langle \widehat{\rm SW}\hat{T}^* \rangle = -\beta_{\rm SW} P_T(\omega) - \frac{\sigma_{\rm SW}^2 + \gamma_{\rm SW}(\gamma_{\rm OLR} + \gamma_{\rm SW} + c_S)P_{\rm ENSO}}{D^*}. \tag{A7b}$$

REFERENCES

Andrews, T., and M. J. Webb, 2018: The dependence of global cloud and lapse rate feedbacks on the spatial structure of tropical Pacific warming. *J. Climate*, **31**, 641–654, https://doi.org/10.1175/JCLI-D-17-0087.1.

——, J. M. Gregory, M. J. Webb, and K. E. Taylor, 2012: Forcing, feedbacks and climate sensitivity in CMIP5 coupled atmosphere–ocean climate models. *Geophys. Res. Lett.*, **39**, L09712, https://doi.org/10.1029/2012GL051607.

——, ——, and ——, 2015: The dependence of radiative forcing and feedback on evolving patterns of surface temperature change in climate models. *J. Climate*, **28**, 1630–1648, https://doi.org/10.1175/JCLI-D-14-00545.1.

Brown, P. T., W. Li, L. Li, and Y. Ming, 2014: Top-of-atmosphere radiative contribution to unforced decadal global temperature variability in climate models. *Geophys. Res. Lett.*, **41**, 5175–5183, https://doi.org/10.1002/2014GL060625.

——, Y. Ming, W. Li, and S. A. Hill, 2017: Change in the magnitude and mechanisms of global temperature variability with warming. *Nat. Climate Change*, **7**, 743–748, https://doi.org/10.1038/nclimate3381.

Chiang, J. C. H., and A. H. Sobel, 2002: Tropical tropospheric temperature variations caused by ENSO and their influence on the remote tropical climate. *J. Climate*, **15**, 2616–2631, https://doi.org/10.1175/1520-0442(2002)015<2616:TTTVCB>2.0.CO;2.

Colman, R., and L. Hanson, 2017: On the relative strength of radiative feedbacks under climate variability and change. *Climate Dyn.*, **49**, 2115–2129,https://doi.org/10.1007/s00382-016-3441-8.

Cooper, F. C., and P. H. Haynes, 2011: Climate sensitivity via a nonparametric fluctuation–dissipation theorem. *J. Atmos. Sci.*, **68**, 937–953, https://doi.org/10.1175/2010JAS3633.1.

Cox, P. M., C. Huntingford, and M. S. Williamson, 2018: Emergent constraint on equilibrium climate sensitivity from global temperature variability. *Nature*, **553**, 319–322, https://doi.org/10.1038/nature25450.

Dalton, M. M., and K. M. Shell, 2013: Comparison of short-term and long-term radiative feedbacks and variability in twentieth-century global climate model simulations. *J. Climate*, **26**, 10 051–10 070, https://doi.org/10.1175/JCLI-D-12-00564.1.

Dessler, A. E., 2010: A determination of the cloud feedback from climate variations over the past decade. *Science*, **330**, 1523–1527, https://doi.org/10.1126/science.1192546.

——, 2013: Observations of climate feedbacks over 2000–10 and comparisons to climate models. *J. Climate*, **26**, 333–342, https://doi.org/10.1175/JCLI-D-11-00640.1.

——, and S. Wong, 2009: Estimates of the water vapor climate feedback during El Niño–Southern Oscillation. *J. Climate*, **22**, 6404–6412, https://doi.org/10.1175/2009JCLI3052.1.

Forster, P. M., T. Andrews, P. Good, J. M. Gregory, L. S. Jackson, and M. Zelinka, 2013: Evaluating adjusted forcing and model spread for historical and future scenarios in the CMIP5 generation of climate models. *J. Geophys. Res. Atmos.*, **118**, 1139–1150, https://doi.org/10.1002/jgrd.50174.

Geoffroy, O., D. Saint-Martin, G. Bellon, A. Voldoire, D. J. L. Olivié, and S. Tytéca, 2013: Transient climate response in a two-layer energy-balance model. Part II: Representation of the efficacy of deep-ocean heat uptake and validation for CMIP5 AOGCMs. *J. Climate*, **26**, 1859–1876, https://doi.org/10.1175/JCLI-D-12-00196.1.

Gregory, J. M., and Coauthors, 2004: A new method for diagnosing radiative forcing and climate sensitivity. *Geophys. Res. Lett.*, **31**, L03205, https://doi.org/10.1029/2003GL018747.

Gritsun, A., and G. Branstator, 2007: Climate response using a three-dimensional operator based on the fluctuation–dissipation theorem. *J. Atmos. Sci.*, **64**, 2558–2575, https://doi.org/10.1175/JAS3943.1.

Hall, A., and X. Qu, 2006: Using the current seasonal cycle to constrain snow albedo feedback in future climate change. *Geophys. Res. Lett.*, **33**, L03502, https://doi.org/10.1029/2005GL025127.

Hasselmann, K., 1976: Stochastic climate models. Part I. Theory. *Tellus*, **28**, 473–485, https://doi.org/10.3402/tellusa.v28i6.11316.

Held, I. M., M. Winton, K. Takahashi, T. Delworth, F. Zeng, and G. K. Vallis, 2010: Probing the fast and slow components of global warming by returning abruptly to preindustrial forcing. *J. Climate*, **23**, 2418–2427, https://doi.org/10.1175/2009JCLI3466.1.

Klein, S. A., B. J. Soden, and N.-C. Lau, 1999: Remote sea surface temperature variations during ENSO: Evidence for a tropical atmospheric bridge. *J. Climate*, **12**, 917–932, https://doi.org/10.1175/1520-0442(1999)012<0917:RSSTVD>2.0.CO;2.

Lau, N.-C., and M. J. Nath, 2001: Impact of ENSO on SST variability in the North Pacific and North Atlantic: Seasonal dependence and role of extratropical sea–air coupling. *J. Climate*, **14**, 2846–2866, https://doi.org/10.1175/1520-0442(2001)014<2846:IOEOSV>2.0.CO;2.

Lloyd, J., E. Guilyardi, and H. Weller, 2012: The role of atmosphere feedbacks during ENSO in the CMIP3 models. Part III: The shortwave flux feedback. *J. Climate*, **25**, 4275–4293, https://doi.org/10.1175/JCLI-D-11-00178.1.

Lutsko, N. J., I. M. Held, and P. Zurita-Gotor, 2015: Applying the fluctuation–dissipation theorem to a two-layer model of quasigeostrophic turbulence. *J. Atmos. Sci.*, **72**, 3161–3177, https://doi.org/10.1175/JAS-D-14-0356.1.

MacMartin, D. G., and E. Tziperman, 2014: Using transfer functions to quantify El Niño Southern Oscillation dynamics in data and models. *Proc. Roy. Soc. London*, **470A**, 20140272, https://doi.org/10.1098/rspa.2014.0272.

MacMynowski, D. G., H.-J. Shin, and K. Caldeira, 2011: The frequency response of temperature and precipitation in a climate model. *Geophys. Res. Lett.*, **38**, L16711, https://doi.org/10.1029/2011GL048623.

Merlis, T. M., I. M. Held, G. L. Stenchikov, F. Zeng, and L. W. Horowitz, 2014: Constraining transient climate sensitivity using coupled climate model simulations of volcanic eruptions. *J. Climate*, **27**, 7781–7795, https://doi.org/10.1175/JCLI-D-14-00214.1.

Murphy, D. M., and P. M. Forster, 2010: On the accuracy of deriving climate feedback parameters from correlations between surface temperature and outgoing radiation. *J. Climate*, **23**, 4983–4988, https://doi.org/10.1175/2010JCLI3657.1.

Percival, D. B., and A. T. Walden, 1993: *Spectral Analysis for Physical Applications: Multitaper and Conventional Univariate Techniques*. Cambridge University Press, 583 pp.

Proistosescu, C., and P. J. Huybers, 2017: Slow climate mode reconciles historical and model-based estimates of climate sensitivity. *Sci. Adv.*, **3**, e1602821, https://doi.org/10.1126/sciadv.1602821.

Rädel, G., T. Mauritsen, B. Stevens, D. Dommenget, D. Matei, K. Bellomo, and A. Clement, 2016: Amplification of El Niño by cloud longwave coupling to atmospheric circulation. *Nat. Geosci.*, **9**, 106–110, https://doi.org/10.1038/ngeo2630.

Ring, M. J., and R. A. Plumb, 2008: The response of a simplified GCM to axisymmetric forcings: Applicability of the fluctuation dissipation theorem. *J. Atmos. Sci.*, **65**, 3880–3898, https://doi.org/10.1175/2008JAS2773.1.

Robert, C., and G. Casella, 2004: *Monte Carlo Statistical Methods*. 2nd ed. Springer, 649 pp.

Soden, B. J., A. J. Broccoli, and R. S. Hemler, 2004: On the use of cloud forcing to estimate cloud feedback. *J. Climate*, **17**, 3661–3665, https://doi.org/10.1175/1520-0442(2004)017<3661:OTUOCF>2.0.CO;2.

——, I. M. Held, R. Colman, K. M. Shell, J. T. Kiehl, and C. A. Shields, 2008: Quantifying climate feedbacks using radiative kernels. *J. Climate*, **21**, 3504–3520, https://doi.org/10.1175/2007JCLI2110.1.

Stevenson, S., B. Fox-Kemper, M. Jochum, B. Rajagopalan, and S. G. Yeager, 2010: ENSO model validation using wavelet probability analysis. *J. Climate*, **23**, 5540–5547, https://doi.org/10.1175/2010JCLI3609.1.

Sun, D.-Z., and Coauthors, 2006: Radiative and dynamical feedbacks over the equatorial cold tongue: Results from nine atmospheric GCMS. *J. Climate*, **19**, 4059–4074, https://doi.org/10.1175/JCLI3835.1.

Wittenberg, A. T., 2009: Are historical records sufficient to constrain ENSO simulations? *Geophys. Res. Lett.*, **36**, L12702, https://doi.org/10.1029/2009GL038710.

Wu, Q., and G. R. North, 2002: Climate sensitivity and thermal inertia. *Geophys. Res. Lett.*, **29**, 1707, https://doi.org/10.1029/2002GL014864.

Xie, S.-P., Y. Kosaka, and Y. M. Okumura, 2016: Distinct energy budgets for anthropogenic and natural changes during global warming hiatus. *Nat. Geosci.*, **9**, 29–33, https://doi.org/10.1038/ngeo2581.

Zhou, C., M. D. Zelinka, A. E. Dessler, and S. A. Klein, 2015: The relationship between interannual and long-term cloud feedbacks. *Geophys. Res. Lett.*, **42**, 10 463–10 469, https://doi.org/10.1002/2015GL066698.

——, ——, and S. A. Klein, 2017: Analyzing the dependence of global cloud feedback on the spatial pattern of sea surface temperature change with a Green's function approach. *J. Adv. Model. Earth Syst.*, **9**, 2174–2189, https://doi.org/10.1002/2017MS001096.